Range-Point Migration-Based Image Expansion Method Exploiting Fully Polarimetric Data for UWB Short-Range Radar

Ayumi Yamaryo, Tatsuo Takatori, Shouhei Kidera, *Member, IEEE*, and Tetsuo Kirimoto, *Senior Member, IEEE*

Abstract—Ultrawideband radar with high-range resolution is a promising technology for use in short-range 3-D imaging applications, in which optical cameras are not applicable. One of the most efficient 3-D imaging methods is the range-point migration (RPM) method, which has a definite advantage for the synthetic aperture radar approach in terms of computational burden, high accuracy, and high spatial resolution. However, if an insufficient aperture size or angle is provided, these kinds of methods cannot reconstruct the whole target structure due to the absence of reflection signals from large part of target surface. To expand the 3-D image obtained by RPM, this paper proposes an image expansion method by incorporating the RPM feature and fully polarimetric data-based machine learning approach. Following ellipsoid-based scattering analysis and learning with a neural network, this method expresses the target image as an aggregation of parts of ellipsoids, which significantly expands the original image by the RPM method without sacrificing the reconstruction accuracy. The results of numerical simulation based on 3-D finite-difference time-domain analysis verify the effectiveness of our proposed method, in terms of image-expansion criteria.

Index Terms—3-D sensors, fully polarimetric analysis, image expansion, range-point migration (RPM), short-range sensing, ultrawideband (UWB) radars.

I. INTRODUCTION

AN ULTRAWIDEBAND (UWB) pulse radar is expected to be adopted in innovative short-range sensing techniques, such as robotic sensors in disaster rescue situations or private watch sensors for independently living elderly or disabled persons. To provide accurate high-resolution 3-D images, researchers have investigated various radar imaging methods based on data synthesis, such as the synthetic aperture radar (SAR) [1], time-reversal algorithms [2], [3], and range migration methods [4]–[6]. However, all of these methods incur impractically large computational costs, particularly in 3-D imaging problems,

and their reconstruction accuracies are insufficient to capture the detailed structures of target shapes. As a different approach, the method [7] has been developed, which is based on reversible transforms, namely, boundary scattering transform. While this method achieves a fast 3-D imaging in specifying boundary extraction, it suffers from serious accuracy degradation in noisy or interfered cases assuming multiple or complex-shaped targets due to being based on the difference operation of observed ranges. In contrast, the range-point migration (RPM) method extracts the 3-D target boundary even in noisy or richly interfered case [8]–[10]. The RPM method assesses the distribution function of the direction of arrival (DOA) for each observed range point (denoted as a set of antenna location and range), and does not require any paring procedure of discrete range points as preprocessing. It also accomplishes highly accurate 3-D imaging for general target shape in far less computation costs compared with that required by conventional signal synthesis approaches such as the 3-D beamforming or SAR-based reconstruction scheme. The effectiveness of RPM has been widely reported in short-range radar and acoustic imaging studies [11]–[13]. However, the image reproduction area obtained by the RPM and other conventional methods is, usually severely limited by an available aperture angle, determined by the aperture size and distance to target, which is itself restricted by obstacles such as rubble in disaster zones and indoor sensing problems. For these reasons, the reconstructed area frequently becomes too narrow to identify the target structure, and this is an essential problem in any kind of imaging methods as far as they use only the direct reflection signal for imaging.

To alleviate this problem, an image expansion method based on ellipse expansion has been proposed [14]. In the method [14], a target, such as human body, is approximated by an aggregate of ellipsoids representing the head, trunk, and limbs; each clustered RPM image is then expanded to a single ellipsoid. The method [14] uniquely computes ellipsoid fitting in data space (constituted by the range points) rather than in real space, avoiding the errors introduced by the RPM imaging process. Although the method [14] accurately expands ellipsoidal targets even in noisy situations, shapes that significantly differ from ellipsoids (such as tori and cylinder) are naturally degraded by the expansion.

To address the above problem, this paper proposes a novel image expansion algorithm by incorporating the RPM feature and fully polarimetric data-based machine learning. Namely, our goal is a more efficient and reliable expansion from the
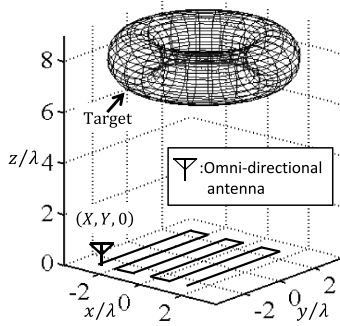
Fig. 1.   System model.

original RPM image with fully polarimetric data. While some studies for incorporating polarimetric data and RPM method, for super-resolution range data extraction [15] or accuracy improvement [16], have been investigated, there are no study for the challenge of image expansion using fully polarimetric data. There are several studies for the polarimetric analysis of the short-range sensing issue [17], [19], [20]. Such literature reveals that the fully polarimetric data exploitation has a possibility to offer a significant improvement for image reconstruction. For more particular investigation for improving the RPM image, this paper tries to relate the fully polarimetric data in the time domain to the target structure focusing on single ellipsoid. According to this analysis, the fully polarimetric data can reveal the axial radii and rotation angles of the ellipsoids. Furthermore, several significant ellipsoidal parameters can be acquired by a neural network (NN) at a single-antenna location.

Finally, we expanded the image from the target points obtained by the RPM method, fitting an aggregation of the partial ellipsoidal surface estimated by the fully polarimetric data to each RPM point. Note that the multiple-partial-ellipsoid-based image expansion, proposed in this paper, is done by exploiting the RPM feature such as one-to-one correspondence between the range point and the target point. This approach fundamentally differs from the conventional one, which relies on fitting a single ellipsoid [14], and is effective for the not-ellipsoidal shape without sacrificing accuracy degradation. Utilized on the data generated by finite-difference time-domain (FDTD) simulations, the proposed method yielded a significantly more expanded target image than did the original RPM method, even for nonelliptical objects.

II. SYSTEM MODEL

Fig. 1 shows the system model. An omnidirectional antenna is scanned on the xy plane, where each location is defined as $(X, Y, 0)$. The monostatic radar is assumed. The transmitted signal as the current source is defined as the monocycle pulse with a center wavelength λ. It assumes the multiple linear polarizations for the x- and y- directions in transmitting and receiving, respectively. $s'_{i,j}(X, Y, t)$ denotes the received electric field at the location $(X, Y, 0)$, at time t, when the transmitting polarization and the receiving polarization are along the $i(x$ or $y)$-axis and $j(x$ or $y)$-axis, respectively. $\tilde{s}_{i,j}(X, Y, t)$ is the output of the Wiener filter of $s'_{i,j}(X, Y, t)$ calculated as

$$\tilde{s}_{i,j}(X, Y, t) = \int_{-\infty}^{\infty} W(\omega) S'_{i,j}(X, Y, \omega) e^{j\omega t} d\omega \tag{1}$$

where $S'_{i,j}(X, Y, \omega)$ is the signal in the frequency domain of $s'_{i,j}(X, Y, t)$. $W(\omega)$ is defined as

$$W(\omega) = \frac{S_{\text{ref}}(\omega)^*}{(1 - \eta)S_0^2 + \eta |S_{\text{ref}}(\omega)|^2} S_0 \tag{2}$$

where $\eta = 1/(1 + (S/N)^{-1})$, and $S_{\text{ref}}(\omega)$ is the reference signal in the frequency domain, which is the complex conjugate of that of the transmitted signal. S_0 is a constant for dimension consistency. This filter is an optimal mean-square-error linear filter for additive noises. $\tilde{s}_{i,j}(X, Y, t)$ is now converted into $s_{i,j}(X, Y, R)$ using $R = ct/2\lambda$, where c is the speed of the radio wave. The range point extracted from the local maxima of $s_{x,x}(X, Y, R)$ as to R is denoted as $\boldsymbol{q} = (X, Y, R)$; the details are given in [8].

III. RPM METHOD AND CONVENTIONAL EXPANSION APPROACH

A. Original RPM Method

We have already established an accurate and high-speed 3-D target boundary extraction method as the RPM method, which can be applicable to various 3-D target shapes having concave surfaces and edge ridges with 1/100 wavelength accuracy [8], [9]. The RPM method method is based on the assumption that a target boundary point (x, y, z) exists on a sphere with its center as the antenna location $(X, Y, 0)$ and its radius as the observed range R. The DOA for each range point $\boldsymbol{q}_i = (X_i, Y_i, R_i)$ can be determined by assessing the spatial accumulation of intersection points of the spheres, whose center is $(X_i, Y_i, 0)$ and radius is R_i. The RPM method determines the target point for the range point $\boldsymbol{q}_i$ as

$$\hat{\boldsymbol{p}}(\boldsymbol{q}_i) = \underset{\boldsymbol{p}^{\text{int}}(\boldsymbol{q}_i; \boldsymbol{q}_l, \boldsymbol{q}_m) \in \mathcal{P}_i}{\arg \max} \sum_{(\boldsymbol{q}_j, \boldsymbol{q}_k) \in \mathcal{Q}_i} g(\boldsymbol{q}_i; \boldsymbol{q}_j, \boldsymbol{q}_k)$$
$$\times \exp\left\{-\frac{\|\boldsymbol{p}^{\text{int}}(\boldsymbol{q}_i; \boldsymbol{q}_j, \boldsymbol{q}_k) - \boldsymbol{p}^{\text{int}}(\boldsymbol{q}_i; \boldsymbol{q}_l, \boldsymbol{q}_m)\|^2}{2\sigma_r^2}\right\} \tag{3}$$

where $\boldsymbol{p}^{\text{int}}(\boldsymbol{q}_i; \boldsymbol{q}_j, \boldsymbol{q}_k)$ denotes the intersection point among the three spheres, determined by the range points $\boldsymbol{q}_i$, $\boldsymbol{q}_j$, and $\boldsymbol{q}_k$. σ_r is an empirically determined constant. Fig. 2 presents the spatial relationship between the three spheres with $\boldsymbol{q}_i$, $\boldsymbol{q}_j$, $\boldsymbol{q}_k$, and its intersection point. The weighting function $g(\boldsymbol{q}_i; \boldsymbol{q}_j, \boldsymbol{q}_k)$ is defined by

$$g(\boldsymbol{q}_i; \boldsymbol{q}_j, \boldsymbol{q}_k) = s(\boldsymbol{q}_j) \exp\left\{-\frac{D(\boldsymbol{q}_i, \boldsymbol{q}_j)^2}{2\sigma_D^2}\right\}$$
$$+ s(\boldsymbol{q}_k) \exp\left\{-\frac{D(\boldsymbol{q}_i, \boldsymbol{q}_k)^2}{2\sigma_D^2}\right\} \tag{4}$$

where $s(\boldsymbol{q}_j)$ denotes the amplitude of $s(\boldsymbol{q}_j)$ at $R = R_j$ and $D(\boldsymbol{q}_i, \boldsymbol{q}_j) = ((X_i - X_j)^2 + (Y_i - Y_j)^2)^{1/2}$ holds. Equation (4) yields the convergence effect of intersection points with respect to the antenna locations. A set of intersection points as $\mathcal{P}_i$ is defined as

$$\mathcal{P}_i = \{\boldsymbol{p}^{\text{int}}(\boldsymbol{q}_i; \boldsymbol{q}_j, \boldsymbol{q}_k) | (\boldsymbol{q}_j, \boldsymbol{q}_k) \in \mathcal{Q}_i\} \tag{5}$$

This article has been accepted for inclusion in a future issue of this journal. Content is final as presented, with the exception of pagination.

YAMARYO *et al.*: RANGE-POINT MIGRATION-BASED IMAGE EXPANSION METHOD
3
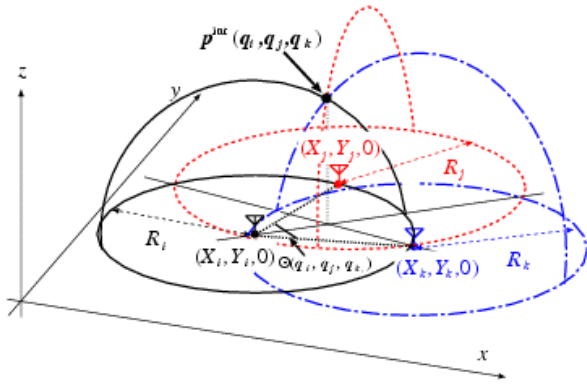
Fig. 2. Relationship among three spheres determined by q_i, q_j, q_k, and its intersection point.

Fig. 3. Observation model for fully polarimetric analysis of a single-ellipsoid target.

where $\mathcal{Q}_i$ denotes the investigating region of antenna locations. Note that each target point denoted as $\hat{p}(q_i)$ is associated with each range point q_i, which means the one-to-one correspondence between them. While the RPM method accomplishes accurate and fast 3-D imaging, even in a richly interfered situation caused by multiple-target reflection or noisy environment, it (also SAR or others) suffers from an insufficient imaging region, when the aperture size is small. This insufficiency is an essential problem in radar imaging methods, and should be resolved by other approaches, such as expansion schemes.

B. Single-Ellipsoid-Based Expansion Method

Here, we briefly introduce the imaging method conventionally used to expand target image regions [14], which is based on an ellipse expansion of an image obtained by RPM. The method [14] performs ellipse fitting in the data space comprising the antenna location and the observed range, which is enabled by the unique feature of RPM imaging [8]. Ellipse fitting of the RPM image in real space is overly sensitive to the errors introduced by the RPM imaging process. In contrast, ellipse fitting in data space is essentially impervious to the imaging error, because the fitting process is directly carried out without the imaging process, whereas RPM is only employed in image clustering. More specifically, the method [14] first uses the target points produced by RPM only for the clustering of the range points, the distribution of which in data space is often very complicated in the case of multiple targets. The clustered range points are then employed for ellipse fitting, which is converted in the data space. However, the method [14] assumes that the target is shaped similar to an ellipse and is inaccurate for significantly dissimilar shapes. The applicability for the nonellipsoidal target, such as the target with edge or having multiple reflection points, has also been demonstrated [8], where the fatal inaccuracy for expansion has been confirmed. This is natural because of a simple assumption that the target should be expressed as a "single" ellipsoid. In addition, multiple targets or complicated target shapes must be correctly clustered; otherwise, serious expansion errors occur.

IV. PROPOSED METHOD

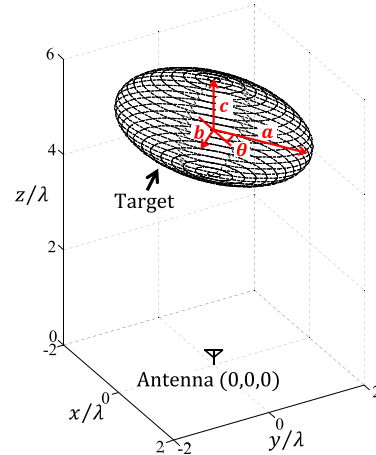This section proposes a novel method that exploits the fully polarimetric data, expanding RPM images to variously shaped targets, and thereby solving the above-mentioned problem. In many studies, significant information on a target structure or a condition has been obtained by analyzing or decomposing multiple polarimetric SAR images [17], [19], [20]. Thus, the potential of utilizing fully polarimetric data in the object or scene detection is well recognized. This paper focuses on the image expansion issue for the reconstructed RPM image, by extracting the polarimetric feature through the time-series data-based NN learning and appropriate fitting algorithm for the nonellipsoidal-shaped target.

A. Polarimetric Analysis of Single-Ellipsoid Target

We first investigate the relationship between the time-series waveform of the fully polarimetric data and ellipsoid parameters (the axial radius and rotation angle). Fig. 3 shows the observation model that is subjected to polarimetric analysis. The target is assumed to be a single ellipsoid centered at $(0, 0, z_c)$. The antenna is located at $(0, 0, 0)$. Here, a, b, and c are the radii of the ellipsoid along the x-axis, y-axis, and z-axis, respectively, and θ is the rotation angle about the z-axis. The observation data are generated by the FDTD method. Fig. 4 shows the Wiener filter output of the received signals $s_{x,x}$, $s_{x,y}$, and $s_{y,y}$ in the time domain, where parameter a is varied while other parameters are fixed ($b = 1.0\lambda$, $c = 0.5\lambda$, and $\theta = 0°$). In this figure, the amplitudes of $s_{x,x}$ and $s_{y,y}$ are positively correlated with the axial radius a of the ellipsoid, while that of $s_{x,y}$ does not significantly change with the axial radius. This fact demonstrates that the amplitude of polarized data along the major axis of an ellipsoid is directly related to the expansion of ellipsoid, where the x-y polarized data do not affect significantly, and this indicates that $s_{x,x}$ and $s_{y,y}$ contribute to the size estimation of the target shape. Fig. 5 shows the Wiener filter output of the received signal $s_{x,y}$ when θ is varied and the other parameters are fixed as $a = 3.0\lambda$, $b = 2.0\lambda$, and $c = 0.5\lambda$. Fig. 5 also shows that an amplitude of $s_{x,y}$ data significantly increases according to target rotation to maximum at 45°. The received amplitude of $s_{x,y}$ strongly correlates with the rotation angle; moreover, the sign of the phase indicates the rotation direction. Therefore,
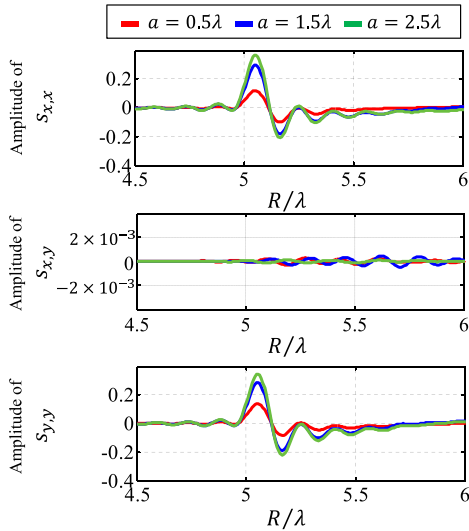
This article has been accepted for inclusion in a future issue of this journal. Content is final as presented, with the exception of pagination.

4

IEEE TRANSACTIONS ON GEOSCIENCE AND REMOTE SENSING

Fig. 4. Outputs of the Wiener filter $s_{x,x}(0,0,R)$, $s_{x,y}(0,0,R)$, and $s_{y,y}(0,0,R)$ when a is a variable and other parameters are fixed as $b = 1\lambda$, $c = 0.5\lambda$, and $\theta = 0°$.
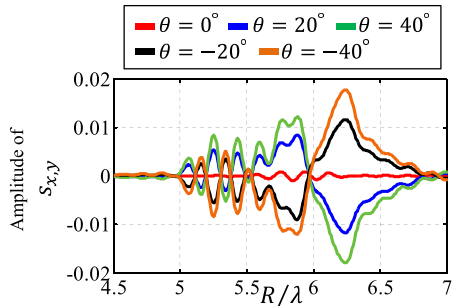

Fig. 5. Outputs of the Wiener filter $s_{x,y}(0,0,R)$ when θ is a variable and other parameters are fixed as $a = 3\lambda$, $b = 2\lambda$, and $c = 0.5\lambda$.

the rotation angle of the ellipsoid can be estimated from the $s_{x,y}$ signal. The fully polarimetric data, especially those of the time-series waveform, contain important information on both the local structure and global expanse of the target shape. Then, one RPM imaging point with no size can be expanded by the partial ellipsoidal surface if such information can be extracted by fully polarimetric data.

B. Neural Network Learning for Fully Polarimetric Data

Based on previous analysis, the proposed method first prepares a time-series data set of various ellipsoids with their a, b, c, and θ parameters. These parameters play an important role in the expansion process, because the proposed method relies on the expansion with an aggregation of ellipsoid. Thus, fully polarimetric data for each range point need to be associated with an ellipsoid, the part of which expresses the local boundary of the actual object. In this method, such an association has been achieved via the NN-based training process as follows. Note that, when one considers the reflection data from the ellipsoid object, there is a creeping wave propagating along the backside of the object. However, the strength of this component is much smaller than that of direct reflection, e.g., specular reflection; then, we deal with the time-series data with a finite length. To generate the input data for the windowed time-series data, we defined an input
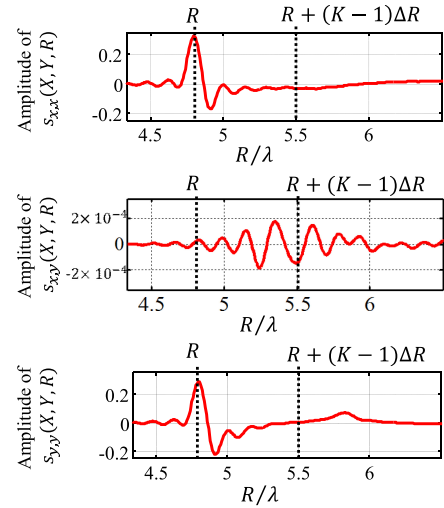

Fig. 6. Extraction scheme for time-series data $s_{x,x}(0,0,R)$, $s_{x,y}(0,0,R)$, and $s_{y,y}(0,0,R)$ in the proposed method.
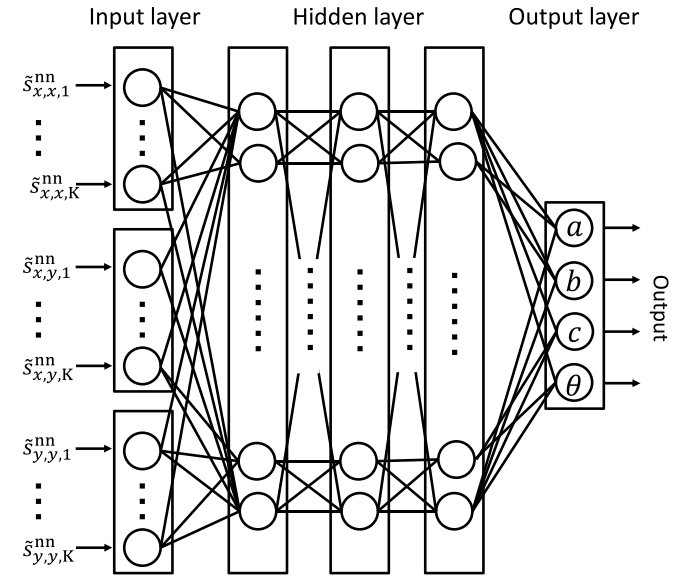

Fig. 7. Layer structure of the NN in the proposed method.

vector $s_{i,j}^{nn}(X,Y,R)(i = x, y, j = x, y)$ for each range point $q = (X, Y, R)$

$$s_{i,j}^{nn}(X,Y,R) \equiv [s_{i,j}(X,Y,R), s_{i,j}(X,Y,R + \Delta R), \ldots, s_{i,j}(X,Y,R + (K-1)\Delta R)] \quad (6)$$

where ΔR corresponds to the time-window scale and K is a constant natural number. Fig. 7 shows the structure of the NN. In the training sequence, the input data of the received signal of the antenna located at $(0, 0, 0)$, namely, $(X, Y) = (0, 0)$, are used, for simplicity, where the ellipsoid parameters (a, b, c, θ) are varied.

These parameters significantly depend on the amplitude of the input signal. Therefore, when inputting the received data into the trained NN, the propagation attenuation of the received amplitude must be considered, because the amplitude directly affects the size of the ellipsoid in the proposed method. The

This article has been accepted for inclusion in a future issue of this journal. Content is final as presented, with the exception of pagination.

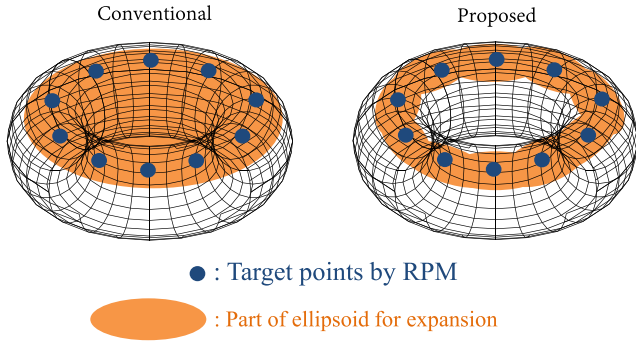YAMARYO *et al.*: RANGE-POINT MIGRATION-BASED IMAGE EXPANSION METHOD

5

Fig. 8. Scheme comparison between the conventional and proposed methods.

proposed method compensates for the propagation attenuation of each received signal by applying a function of the measured range R. Theoretically, the amplitude of a signal radiated from a point source is attenuated on the first order of the propagation range. However, in this case, we must consider the reflection signals from various shapes of target, and it is generally difficult to estimate an attenuation ratio without the knowledge of the target shape, theoretically. To address this problem, we investigated the attenuation ratios from various ellipsoids at various distances and calculated the average attenuation ratio. Specifically, the distance from an ellipsoid target to the antenna was rescaled as 1.0λ to 10λ in the 1.0λ interval. The antenna was located at $(0, 0, 0)$, and the observation data are also generated by FDTD. The ellipsoid was postured as shown in Fig. 3. The ellipsoid parameters a, b, and c are each varied as 0.5λ, 1λ, 1.5λ, 2λ, 2.5λ, and 3λ, while $\theta = 0°$ is fixed.

The input time-series data $\tilde{s}_{i,j}^{\text{nn}}(X, Y, R)(i = x, y, j = x, y)$ are then compensated as

$$\tilde{s}_{i,j}^{\text{nn}}(X, Y, R) = f(R/R_0)s_{i,j}^{\text{nn}}(X, Y, R_0) \tag{7}$$

where $f(R/R_0)$ denotes the averaged attenuation ratio and R_0 is the reference distance. Note that $f(R/R_0)$ is a polynomial function of R/R_0, which is fitted to the logarithm of the above-described data set.

C. Multiple-Ellipsoid-Based Image Expansion for RPM Point

Our image expansion methodology relies on fitting each RPM target point to a partial ellipsoidal surface with parameters estimated by the above NN approach. In the literature [14], each group of target points obtained by RPM was expanded as a single ellipsoid, which is problematic for shapes that widely differ from ellipsoids. Thus, the proposed method expresses each RPM target point as part of an ellipsoid surface, that is, a single target shape is expressed as an aggregation of partial ellipsoidal surfaces. Fig. 8 shows the difference between the conventional and proposed schemes for image expansion. In this sense, our method differs from that in [14]. Fig. 9 illustrates the basic concept of the multiple ellipsoid-based expansion scheme. In the proposed method, the part of each ellipsoid (estimated by each q_k through the trained NN) is fitted to each RPM point as p_k, using the line-of-sight (LOS) direction e_k^n. Note that, to avoid overfitting, only a portion of the ellipsoid is used for image expansion.
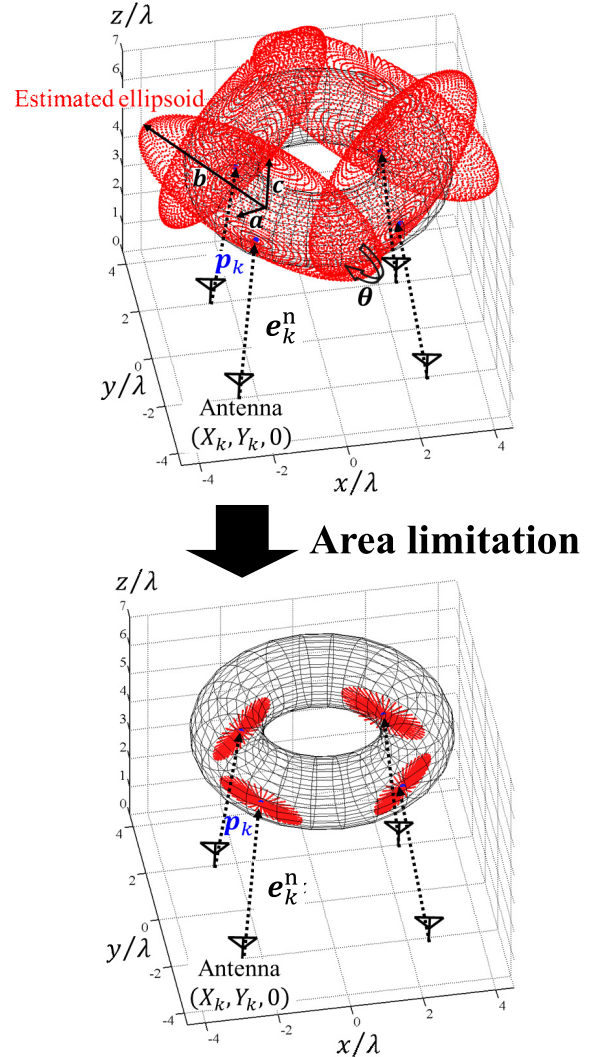

Fig. 9. Example of the expanded result by the proposed method.

For appropriate fitting of the partial ellipsoid, the ellipsoid boundary points are converted to fit the RPM point and its LOS direction as

$$\begin{pmatrix} x_k^E \\ y_k^E \\ z_k^E \end{pmatrix} = \begin{pmatrix} \cos\hat{\theta} & -\sin\hat{\theta} & 0 \\ \sin\hat{\theta} & \cos\hat{\theta} & 0 \\ 0 & 0 & 1 \end{pmatrix} \begin{pmatrix} \hat{a}\cos\phi\cos\psi \\ \hat{b}\cos\phi\sin\psi \\ \hat{c}\sin\psi \end{pmatrix}$$
$$+ \begin{pmatrix} 0 \\ 0 \\ R_k - (z_c - \hat{c}/2) \end{pmatrix} \tag{8}$$

where $(\hat{a}, \hat{b}, \hat{c}, \hat{\theta})$ is estimated parameters for the range points q_k, and ϕ and ψ are the azimuthal and elevation angles of the ellipsoid, respectively. To determine the ellipsoid for each target point, we need to estimate the 9 degree of freedom. In this case, we investigate four independent parameters a, b, c, and ϕ, and need to determine other five parameters from the RPM point and its geometrical characteristic. Here, applying RPM to the range points $q_k = (X_k, Y_k, R_k)$, we also estimated a corresponding target point $p_k = (x_k, y_k, z_k)$. Note that each target point p_k satisfies a one-to-one correspondence with each range point q_k; this feature is unique to RPM

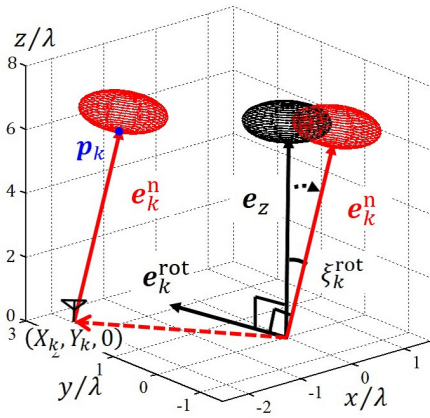This article has been accepted for inclusion in a future issue of this journal. Content is final as presented, with the exception of pagination.

6

IEEE TRANSACTIONS ON GEOSCIENCE AND REMOTE SENSING

Fig. 10. Ellipsoid rotation and translation along the LOS direction e_k^n.

Fig. 11. Relationship between $\Delta x / \Delta X$ and curvature of the target surface.

imaging. Under the assumption that the antenna receives a strong echo from the target boundary, which is perpendicular to the LOS direction on p_k, the unit vector of the LOS direction, that is, the normal vector on the target boundary, is calculated as $e_{n,k} = (p_k - (X_k, Y_k, 0))/\|p_k - (X_k, Y_k, 0)\|$. In addition, since the target boundary should be tangent to the plane orthogonal to this normal vector, the expanding ellipsoid should also be tangent to the target boundary. Even in this geometrical condition, the total parameters of the ellipsoid cannot be uniquely determined; then, for simplicity, we assume that the tangential point of each ellipsoid is located at an elevation angle $\psi = -\pi/2$.

Then, the LOS direction in the learning process as in Fig. 3, namely, $e_z = (0, 0, 1)$, is converted to that for each range point q_k according to e_k^n. According to conversion, each point (x_k^E, y_k^E, z_k^E) on the estimated ellipsoid boundary is also converted as

$$\left(\tilde{x}_k^E, \tilde{y}_k^E, \tilde{z}_k^E \right)^T = R_k\left(e_k^{\text{rot}}, \xi_k^{\text{rot}} \right)\left(x_k^E, y_k^E, z_k^E \right)^T + (X_k, Y_k, 0)^T \tag{9}$$

where the matrix $R_k(e_k^{\text{rot}}, \xi_k^{\text{rot}})$ denotes 3-D rotation along the axis $e_k^{\text{rot}} = ((e_z \times e_k^n)/(\|e_z \times e_k^n\|))$ with the angle $\xi_k^{\text{rot}} = \cos^{-1}(e_z \cdot e_k^n)$. Specifically, the matrix is calculated as (10), as shown at the bottom of the page.

where $e_k^{\text{rot}} = (e_{x,k}^{\text{rot}}, e_{y,k}^{\text{rot}}, e_{z,k}^{\text{rot}})$ and $C_k = 1 - \cos \xi_k^{\text{rot}}$. Fig. 10 illustrates the translation and rotation of the ellipse so as to fit the target point p_k.

Finally, a part of the ellipsoid is extracted as $\hat{\Omega}_k$ for each q_k. To accomplish an edge-preserving property in the expansion process, the proposed method changes the size of the portion of the ellipsoid, corresponding to the curvature radius of the target surface. The literature [22] or [23] revealed that the following matrix can assess the curvature radius along each axis:
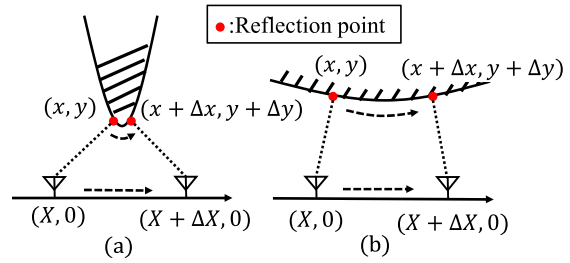
$$S_k = \begin{bmatrix} \dfrac{\partial x_k}{\partial X_k} & \dfrac{\partial y_k}{\partial X_k} \\ \dfrac{\partial x_k}{\partial Y_k} & \dfrac{\partial y_k}{\partial Y_k} \end{bmatrix} \simeq \begin{bmatrix} \dfrac{\Delta x_k}{\Delta X_k} & \dfrac{\Delta y_k}{\Delta X_k} \\ \dfrac{\Delta x_k}{\Delta Y_k} & \dfrac{\Delta y_k}{\Delta Y_k} \end{bmatrix} \tag{11}$$

where (x_k, y_k, z_k) denotes the target boundary point estimated by RPM corresponding to $q_k = (X_k, Y_k, R_k)$. Note that each difference approximation in the right-hand term in 11 is readily calculated by using the one-to-one relationship between q_k and (x_k, y_k, z_k). Fig. 11 shows the relationship between object boundaries with a small or large curvature radius, and the value of $\partial y_k / \partial X_k$ in the 2-D view. As shown in Fig. 11, $\partial y_k / \partial X_k$ can approximately and simply assess the curvature radius indirectly. Then, the parameter for the expansion area is calculated as follows:

$$\phi_k(\psi) = \sqrt{u_k(\psi)^2 + v_k(\psi)^2}\, \phi_E \quad (0 \le \psi \le 2\pi) \tag{12}$$

$$(u_k(\psi) \quad v_k(\psi))^T = U_k(\lambda_{1,k} \cos(\psi) \quad \lambda_{2,k} \sin(\psi))^T \tag{13}$$

where ψ and $\phi_k(\psi)$ denote the elevation and azimuth angles of an expanded ellipsoid, respectively. $\lambda_{1,k}$ and $\lambda_{2,k}$ are the eigenvalues of S_k, which determine the principal curvature of (x_k, y_k, z_k), and U_k is the matrix consist of the eigenvectors of S_k. ψ_E is determined empirically. This process enables us to change an expansion area depending on its curvature, namely, an edge-preserving is possible.

Then, the expanded image $\hat{\Omega}_{\text{ex}}$ is determined as

$$\hat{\Omega}_{\text{ex}} = \bigcup_k \hat{\Omega}_k. \tag{14}$$

The bottom side of Fig. 9 denotes the area-limitation example, described above.

After training process through the NN with the FDTD data, the actual imaging process in the proposed method is summarized as follows.

Step 1): Target boundary points $p_k = (x_k, y_k, z_k)(k = 1, \ldots, N_{\text{RP}})$ are obtained by applying the RPM to $q_k = (X_k, Y_k, R_k)$, which is extracted from the local maximum of $s_{x,x}(X_k, Y_k, R_k)$.

$$R_k\left(e_k^{\text{rot}}, \xi_k^{\text{rot}} \right) = \begin{pmatrix} C_k \left(e_{x,k}^{\text{rot}} \right)^2 + \cos \xi_k^{\text{rot}} & C_k e_{x,k}^{\text{rot}} e_{y,k}^{\text{rot}} - e_{z,k}^{\text{rot}} \sin \xi_k^{\text{rot}} & C_k e_{z,k}^{\text{rot}} e_{x,k}^{\text{rot}} + e_{y,k}^{\text{rot}} \sin \xi_k^{\text{rot}} \\ C_k e_{z,k}^{\text{rot}} e_{x,k}^{\text{rot}} - e_{y,k}^{\text{rot}} \sin \xi_k^{\text{rot}} & C_k \left(e_{y,k}^{\text{rot}} \right)^2 + \cos \xi_k^{\text{rot}} & C_k e_{y,k}^{\text{rot}} e_{z,k}^{\text{rot}} - e_{x,k}^{\text{rot}} \sin \xi_k^{\text{rot}} \\ C_k e_{z,k}^{\text{rot}} e_{x,k}^{\text{rot}} - e_{y,k}^{\text{rot}} \sin \xi_k^{\text{rot}} & C_k e_{y,k}^{\text{rot}} e_{z,k}^{\text{rot}} + e_{x,k}^{\text{rot}} \sin \xi_k^{\text{rot}} & C_k \left(e_{z,k}^{\text{rot}} \right)^2 + \cos \xi_k^{\text{rot}} \end{pmatrix} \tag{10}$$
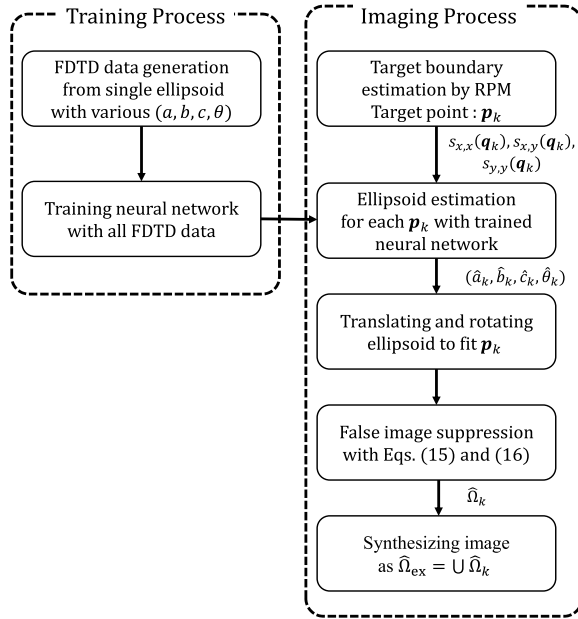
This article has been accepted for inclusion in a future issue of this journal. Content is final as presented, with the exception of pagination.

YAMARYO *et al.*: RANGE-POINT MIGRATION-BASED IMAGE EXPANSION METHOD

7

Fig. 12.   Flowchart of the proposed method.

TABLE I

ESTIMATION RESULTS FOR THE NN-BASED
PARAMETER ESTIMATION OF A SINGLE ELLIPSOID

True $(a/\lambda, b/\lambda, c/\lambda, \theta/\deg)$	Estimated $(a/\lambda, b/\lambda, c/\lambda, \theta/\deg)$	Relative error (a, b, c, θ)[%]
(1.70,1.00,2.50,30.0)	(1.72,0.97,2.51,28.0)	(1.14,2.68,0.28,6.76)
(1.50,2.20,3.00,20.0)	(1.51,2.18,3.00,21.7)	(0.85,0.73,0.05,8.53)
(1.00,2.00,2.70,40.0)	(1.01,2.01,2.69,43.2)	(0.62,0.56,0.24,7.99)
(2.00,1.50,1.00,-35.0)	(2.02,1.48,0.97,-37.0)	(0.97,1.48,3.48,5.39)
(1.40,2.80,2.00,10.0)	(1.40,2.82,2.01,9.6)	(0.33,0.64,0.36,3.68)
(2.30,1.50,1.10,20.0)	(2.38,1.47,1.09,19.1)	(3.39,2.18,1.07,4.34)
(2.80,2.50,0.50,25.0)	(2.64,2.67,0.53,20.7)	(5.87,6.77,5.92,17.34)
(3.00,1.70,0.90,30.0)	(3.22,1.78,0.85,28.2)	(7.48,4.97,5.27,6.15)
(2.50,1.30,2.00,13.0)	(2.53,1.32,2.04,14.0)	(1.20,1.82,2.03,7.48)
(1.00,2.00,2.40,-15.0)	(1.02,2.01,2.39,-14.9)	(1.76,0.67,0.22,0.55)
(2.80,1.70,1.10,35.0)	(2.81,1.74,1.16,36.6)	(0.35,2.46,5.00,4.57)

method. In addition, the proposed method does not need any clustering scheme for RPM points in advance, which is required in [14]. This is because each ellipsoid is independently assigned to each target point.

V. PERFORMANCE EVALUATION IN NUMERICAL SIMULATION

This section describes two types of performance evaluations. One is the evaluation of NN-based learning using fully polarimetric data, where unknown parameters of ellipsoid are estimated by the NN with the time-series database. The other demonstrates the performance of image expansion by our proposed method, namely, multiple-ellipsoid-based expansion for RPM imaging points.

A. Ellipsoid Parameter Estimation by Neural Network

This section reports on the parameter estimation of a single ellipsoid from the fully polarimetric data set. The antenna is located at $(x, y, z) = (0, 0, 0)$. During the learning stage of the NN, the parameters a, b, and c of the training ellipsoids are varied as 0.5λ, 1λ, 1.5λ, 2λ, 2.5λ, and 3λ, and θ is varied as $-40°$, $-30°$, $-20°$, $-10°$, $0°$ $10°$, $20°$, $30°$, and $40°$, respectively. All of these a, b, c, and θ, namely, 1944 different combinations are used as the training data. The conductivity and relative permittivity of the ellipsoid target are set to 1.0×10^7 S/m and $\epsilon = 1.0$, respectively. The observation data are generated by the FDTD method assuming a noiseless situation. The NN contains three hidden layers, with 30 neurons in the first layer, 20 in the second layer, and 10 in the final layer. Here, $K \Delta R = 1.44\lambda$, and the sample interval of the range as $\Delta R = 0.03\lambda$ is set in (6). Table I lists the parameters of the ellipsoid targets estimated by the trained NN. The untrained parameters are depicted in red font. From Table I, it can be observed that the time-series-based NN accurately estimated the ellipsoidal parameters. The average relative errors in a, b, c, and θ are 2.7%, 2.3%, 1.3%, and 6.9%, respectively.

B. Expansion Performance

This section presents the expansion results of our proposed method. The transmitting and receiving antenna sets are scanned over the area $-2.5\lambda \leq x, y \leq 2.5\lambda$ at 0.5λ intervals in the x- and y-directions. Again, the observation

Step 2): $s_{i,j,k}^{nn}(X, Y, R)$ for q_k (uniquely connected with p_k) are extracted as in (6), and are compensated as $\tilde{s}_{i,j,k}^{nn}(X, Y, R)$ in (7) corresponding to the observation distance R_k.

Step 3): $\tilde{s}_{i,j,k}^{nn}(X, Y, R)$ is inputted to the trained NN for obtaining the parameters of the ellipsoid as $(\hat{a}_k, \hat{b}_k, \hat{c}_k, \hat{\theta}_k)$.

Step 4): Each estimated ellipsoid denoted as (x_k^E, y_k^E, z_k^E) is rotated and translated as $(\tilde{x}_k^E, \tilde{y}_k^E, \tilde{z}_k^E)$ so that it fits each target point $p_k = (x_k, y_k, z_k)$ in (9), and its partial area as $\hat{\Omega}_k$ is extracted.

Step 6): For all range points q_k, Steps 2) and 5) are carried out and an expanded image as $\hat{\Omega}_k$ is generated.

Step 7): For the l-th discrete member belonging in $\hat{\Omega}_k$, denoted as $p_{k,l}^E$, the following evaluation function is introduced:

$$\zeta(p_{k,l}^E) = \sum_{m,n,(m \neq k)} \exp \left\{ -\frac{\| p_{k,l}^E - p_{m,n}^E \|^2}{2\sigma_\zeta^2} \right\}. \quad (15)$$

If the following condition is satisfied:

$$\zeta(p_{k,l}^E) \leq \gamma \max_{m,n} \zeta(p_{m,n}^E). \quad (16)$$

The point $p_{k,l}^E$ is removed from $\hat{\Omega}_k$. The final expanded image $\hat{\Omega}_{ex}$ is expressed as an aggregate of $\hat{\Omega}_k$ as in (14).

Fig. 12 outlines the flowchart of the proposed method. Note that the postprocedure in Step 7) eliminates the large deviated points in considering the spatial density of all expanded imaging points as $p_{k,l}^E$. The parameter σ_ζ can be determined by considering the assumed sampling interval of each discrete-formed ellipsoid. As in this flowchart, once the NN learned the training data generated by the FDTD, the proposed method does not require the FDTD or NN training process for each imaging, which maintains high-speed 3-D imaging with this

This article has been accepted for inclusion in a future issue of this journal. Content is final as presented, with the exception of pagination.

8

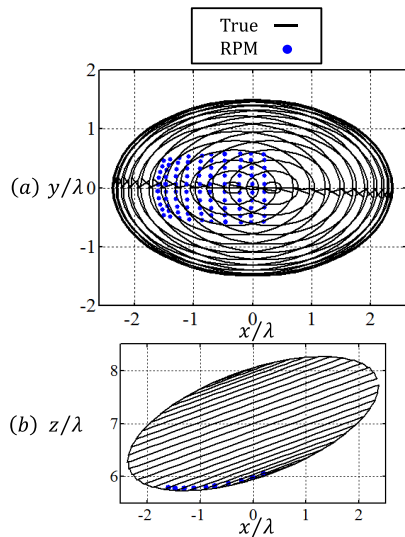IEEE TRANSACTIONS ON GEOSCIENCE AND REMOTE SENSING

Fig. 13. Target boundary points estimated by the RPM method for a single-ellipsoid target in a noiseless situation. (a) Projection to the xy plane. (b) Cross section of the $y = 0$ plane. Solid lines: discrete expression of the true boundary.
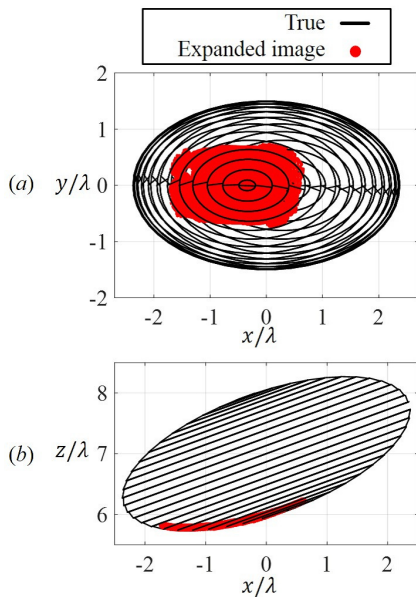

Fig. 14. Expansion result of the proposed method for a single-ellipsoid target in a noiseless situation. (a) Projection to the xy plane. (b) Cross section of the $y = 0$ plane. Solid lines: discrete expression of the true boundary.

data are generated by the FDTD method. Here, the operational frequency band (10-dB criteria mostly used in the UWB signal) in this simulation is about 2.0 GHz, and its range resolution is 150 mm. The center frequency is 3 GHz (the corresponding wavelength in the air is 100 mm), denoting that its fractional bandwidth is around 66%.

In RPM imaging, the set of range points $\boldsymbol{q}_{x,x}$ extracted by $s_{x,x}(X, Y, R')$ is used only in initial 3-D imaging. Fig. 13 shows the target points obtained by RPM for the ellipsoid target, where the solid lines show the discrete expression of the true ellipsoidal boundary. Here, $a = 2.5\lambda$, $b = 1.5\lambda$, $c = 1.0\lambda$, $\theta = 0°$, and the y-axis is rotated through 20°. According to Fig. 13, the target points obtained by RPM cannot sufficiently express the target image to recognize the original ellipsoidal
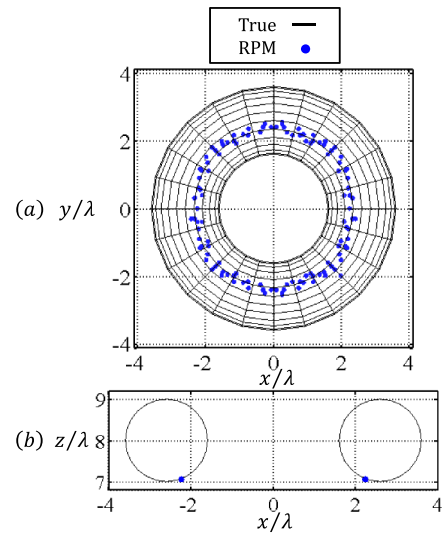

Fig. 15. Target boundary points estimated by the RPM method for the torus target in a noiseless situation. (a) Projection to the xy plane. (b) Cross section of the $y = 0$ plane. Solid lines: discrete expression of the true boundary.
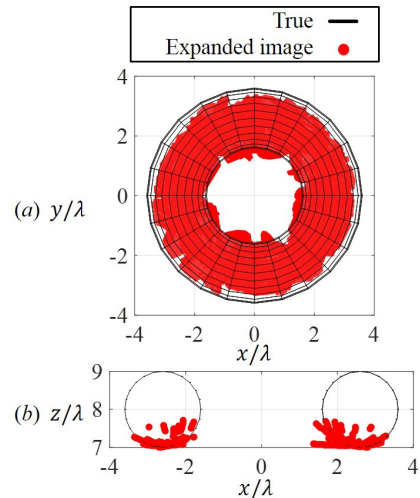

Fig. 16. Expansion result of the proposed method for the torus target in a noiseless situation. (a) Projection to the xy plane. (b) Cross section of the $y = 0$ plane. Solid lines: discrete expression of the true boundary.

shape, while a highly reconstruction accuracy is provided. This is because the target is located from the sensor location with a significant distance around 6λ, and this leads to smaller aperture angle. On the contrary, Fig. 14 shows the image expansion result obtained by the proposed method. Here, the elevation angle of each ellipsoid is limited to ($\phi_E = -7\pi/18$). Also, the parameter $\sigma_\zeta = 0.25\lambda$ and $\gamma = 0.3$ in (15) are set. Fig. 14 indicates that the proposed method correctly expands the target points obtained from the RPM imaging points. Figs. 15 and 16 show the target points obtained by RPM and the expansion expression of the proposed method, respectively. The target is the torus shown in Fig. 1. According to these figures, the proposed method significantly enhances the imaging region of the torus boundary, which is dissimilar to an ellipsoid. The expansion errors in Fig. 16 result from the inaccurate estimation of the ellipsoid parameters from time-series data, because each antenna receives multiple reflection

This article has been accepted for inclusion in a future issue of this journal. Content is final as presented, with the exception of pagination.

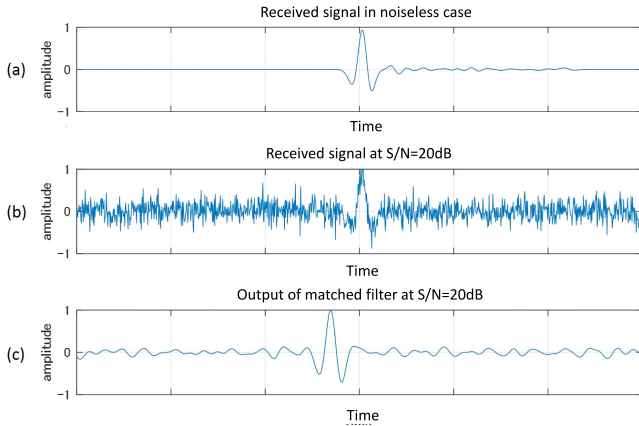YAMARYO *et al.*: RANGE-POINT MIGRATION-BASED IMAGE EXPANSION METHOD

9

Fig. 17. Example of the received signal. (a) Received signal in a noiseless case. (b) Received signal in $S/N = 20$ dB. (c) Output of the matched filter for a received signal illustrated in (b).

Fig. 18. Target boundary points estimated by the RPM method for an ellipsoid target in $S/N = 20$ dB. (a) Projection to the xy plane. (b) Cross section of the $y = 0$ plane. Solid lines: discrete expression of the true boundary.

Fig. 19. Expansion result of the proposed method for an ellipsoid target in $S/N = 20$ dB. (a) Projection to the xy plane. (b) Cross section for the $y = 0$ plane. Solid lines: discrete expression of the true boundary.

echoes within range resolution from the torus boundary, and then, the expansion accuracy depends on the operational bandwidth, naturally. It should be considered that an another cause is the convex boundary based fitting with ellipsoid, namely, the positive principal curvature, while the part of the torus boundary has a negative principal curvature, such as the saddle boundary. However, a largely deviated artifact of the part of the expansion image is efficiently suppressed by introducing postprocessing denoted in Step 7) in the proposed method. It should also be noted that there is accuracy degradation caused by the discrepancy between the reference signal and the actual received signal in the ranging process with Wiener filtering. However, such a kind of ranging inaccuracy is in the order of 0.1λ, and affects both the RPM and the proposed methods [21], [22]. To prevent this interference effect, the windowing time span for extracting the time-series data should be also appropriately determined. The average calculation times for the original RPM and the proposed method after NN learning are 0.2 and 30 s, respectively, using the Intel Xeon CPU E5-1620 v2 3.70-GHz processor, and such a calculation time is hardly achieved by the conventional beamforming or Kirchhoff migration algorithms in obtaining the 3-D full image.

We now discuss a noisy situation. Each received signal is subjected to Gaussian white noises $s_{x,x}$, $s_{x,y}$, and $s_{y,y}$. The signal-to-noise ratio (S/N) is defined as the ratio of the peak instantaneous signal power in all polarization data to the average noise power after applying a matched filter. Fig. 18 shows the RPM-obtained target points of a single ellipsoid in the noisy case. The average S/N of $s_{x,y}$ is approximately 20 dB and those of $s_{x,x}$ and $s_{y,y}$ are approximately 50 dB. It should be noted that the above definition is the strictest estimation for S/N, because the matched filter is the most noise-robust filter, namely, this definition considers the locality of the signal in both the time and frequency domains. Fig. 17 shows an example of received signals assuming $S/N = 20$ dB, and it denotes that while the signal can be recognized after applying the matched filter [denoted as Fig. 17(c)], the raw received signal in Fig. 17(b) (before applying the matched filter) is more noisy. Such an S/N level signal is usually obtained in the real experiment assuming short-range sensing
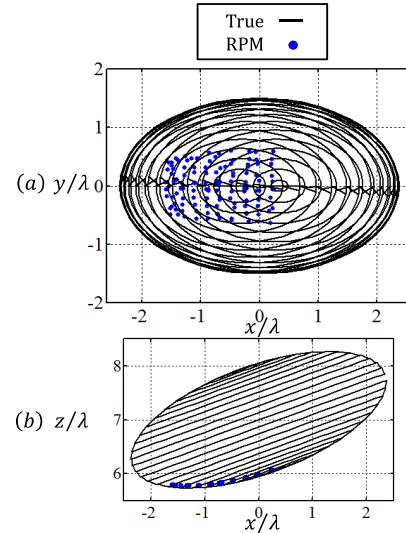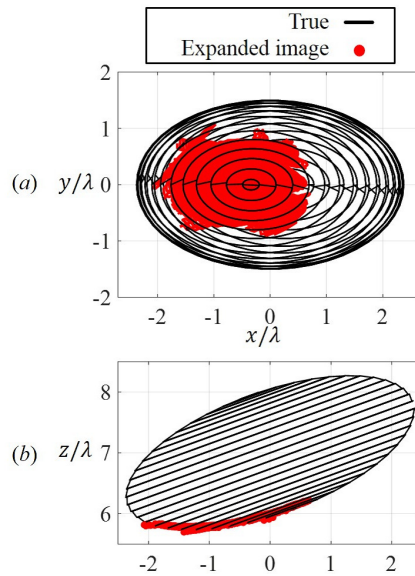
(distance from the sensor is within 5 m), as demonstrated in [10].

Fig. 18 indicates that the RPM retains sufficient accuracy even in a noisy situation, while the estimated points express only a portion of the whole target shape. Fig. 19 shows the expansion results of the proposed method. Although the expansion accuracy is slightly worse than that in the noiseless situation, the proposed method significantly expanded the region that can be imaged, while maintaining an acceptable accuracy. Figs. 20 and 21 show the results of imaging a torus by RPM and by the proposed expansion method, respectively. The approximate average S/N values of $s_{x,y}$, $s_{x,x}$, and $s_{y,y}$ are 20, 32, and 32 dB, respectively. Comparing these results with the noiseless case, the noise did not severely degrade
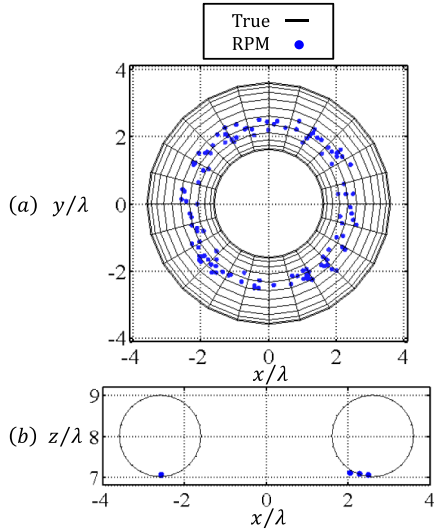
This article has been accepted for inclusion in a future issue of this journal. Content is final as presented, with the exception of pagination.

10   IEEE TRANSACTIONS ON GEOSCIENCE AND REMOTE SENSING

Fig. 20. Target boundary points estimated by the RPM method for the torus target in $S/N = 20$ dB. (a) Projection to the xy plane. (b) Cross section of the $y = 0$ plane. Solid lines: discrete expression of the true boundary.

Fig. 21. Expansion result of the proposed method for the torus target in $S/N = 20$ dB. (a) Projection to the xy plane. (b) Cross section of the $y = 0$ plane. Solid lines: discrete expression of the true boundary.
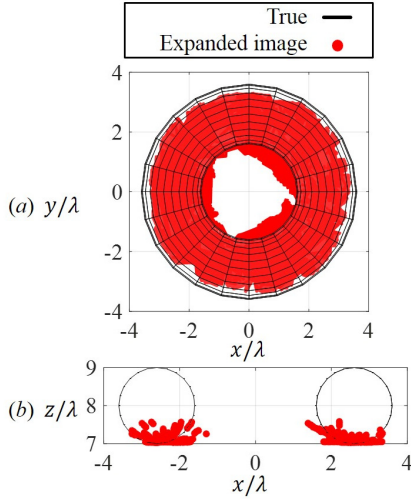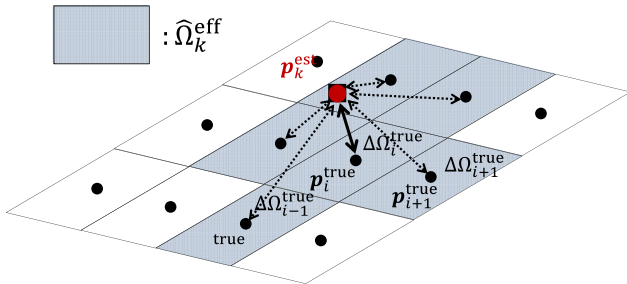

Fig. 22. Spatial relationship of the effective image area $\hat{\Omega}_k^{\text{eff}}$ for each target point $\boldsymbol{p}_k^{\text{est}}$.

the image expansion, and the expansion of the image is retained.

Finally, the image expansion is quantitatively analyzed by investigating the effective reconstruction image region, namely, the expansion effect. For this evaluation, first, a whole true target boundary denoted as $\Omega_{\text{all}}^{\text{true}}$ is divided into small

TABLE II
VALUE OF $P_a[\%]$ OF EACH METHOD

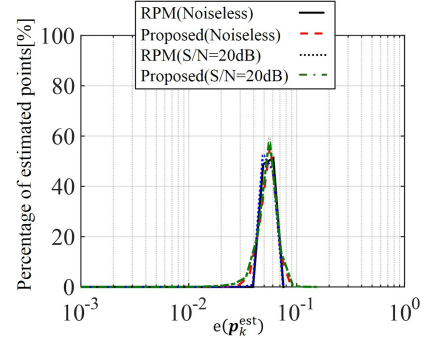| S/N	∞		20dB$(s_{x,y})$	
Target	Ellipsoid	Torus	Ellipsoid	Torus
RPM	15.9 %	7.2 %	16.3 %	7.6 %
Proposed	21.6 %	34.9 %	26.7 %	35.4 %

Fig. 23. Number of the estimated target points of the ellipse target in noiseless and noisy situations.

regions with the same area as $\Delta\Omega_i^{\text{true}}$, $(i = 1, 2, \ldots, N_{\text{tar}})$. A whole target boundary region is expressed as

$$\Omega_{\text{all}}^{\text{true}} = \bigcup_i \Delta\Omega_i^{\text{true}}. \qquad (17)$$

Also, the center point for the region Ω_i^{true} is defined as $\boldsymbol{p}_i^{\text{true}}$. Then, for the kth estimated target point denoted as $\boldsymbol{p}_k^{\text{est}}$, the estimated effective image area $\hat{\Omega}_k^{\text{eff}}$ is defined as

$$\hat{\Omega}_k^{\text{eff}} = \left\{ \bigcup_i \Delta\Omega_i^{\text{true}} \middle| \left\| \boldsymbol{p}_i^{\text{true}} - \boldsymbol{p}_k^{\text{est}} \right\| \leq \delta_p \right\} \qquad (18)$$

where δ_p is the threshold for extracting the effective image region, which is empirically determined as $\delta_p = 0.2\lambda$, in this case. The effective image area $\hat{\Omega}^{\text{eff}}$ composed of all target points is defined as

$$\hat{\Omega}^{\text{eff}} = \bigcup_k \hat{\Omega}_k^{\text{eff}}. \qquad (19)$$

As the evaluation value for the image expansion effect, the image expansion ratio is defined as

$$P_a = \frac{S_{\text{eff}}}{S_{\text{true}}} \qquad (20)$$

where S_{true} and S_{eff} denote the areas of $\Omega_{\text{all}}^{\text{true}}$ and $\hat{\Omega}^{\text{eff}}$, respectively. Fig. 22 illustrates for the effective image area $\hat{\Omega}_k^{\text{eff}}$ for each target point $\boldsymbol{p}_k^{\text{est}}$. The percentage image expansion ratio P_a in the absence and presence of noise is computed for each method, and the results are summarized in Table II. Clearly, the proposed method significantly expands the target image, even when the target deviated from an ellipsoid.

However (see also Figs. 16 and 21), in the case of torus-shaped target, there are nonnegligible errors in expansion. Although it significantly enhances the image expansion ratio, the expansion accuracy requires an additional evaluation criterion. The error in image reconstruction is given by

$$e\left(\boldsymbol{p}_k^{\text{est}}\right) \equiv \min_{\boldsymbol{p}_{\text{true}}} \left\| \boldsymbol{p}_k^{\text{est}} - \boldsymbol{p}^{\text{true}} \right\| \quad (k = 1, 2, \ldots, N_{\text{est}}) \qquad (21)$$
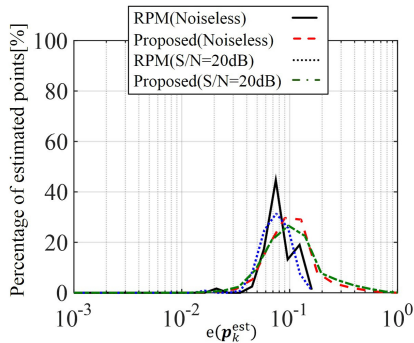
Fig. 24. Number of the estimated target points of the torus target in noiseless and noisy situations.

TABLE III
RATE OF ESTIMATED TARGET POINTS THAT SATISFY $e \leq 0.2\lambda$

S/N	∞		20dB($s_{x,y}$)	
Target	Ellipsoid	Torus	Ellipsoid	Torus
RPM	100 %	100 %	100.0 %	100 %
Proposed	100 %	94.3 %	100 %	90.6 %

where p^{true} denotes the true target points in discrete expression with sufficiently dense sample and N_{est} denotes the total number of the estimated points. Figs. 23 and 24 plot the number of estimated points with error $e(p_k^{\text{est}})$ in the expansions of ellipsoidal and toroidal targets, respectively. While the proposed method and RPM yield the same reconstruction accuracy of ellipsoidal targets, RPM better reconstructs the toroidal target because of the aforementioned interference effect in the proposed method. However, the maximum error in the toroidal target is within 1 λ, and the apparent expanded image does not markedly deviate from the actual target shape. Table III lists the percentage of estimated target points satisfying $e(p_k^{\text{est}}) \leq 0.2\lambda$ in the ellipsoidal and toroidal cases. Combining this evaluation and the image expansion ratio denoted as P_a shown in Table II, the proposed method achieves an effective target image expansion without sacrificing a serious accuracy degradation. Clearly, the percentage of accurately estimated target points (expanded points) is reduced when our method is applied to toroidal objects. This inaccuracy must be addressed in our future work.

C. Evaluation of Edge-Preserving Property

To demonstrate the edge-preserving property of the proposed method, this section introduces the example for the cylinder-shaped target. Figs. 25 and 26 show the RPM-obtained target points and the expanded image by the proposed method, respectively. A noiseless situation is assumed. As shown in Fig. 25, the RPM holds a high accuracy even around the end of the cylinder target, but expresses a part of the cylinder shape. Fig. 26 shows that our proposed method expands the cylinder shape without over expansion of the edge region, where the expansion area is limited along a larger curvature direction in (13). The ratio that the reconstructed points satisfy is that the errors less than 0.2λ are 100% for both the conventional and proposed methods. The image expansion ratios denoted as P_a are 6.9% for the original RPM and 14.4%
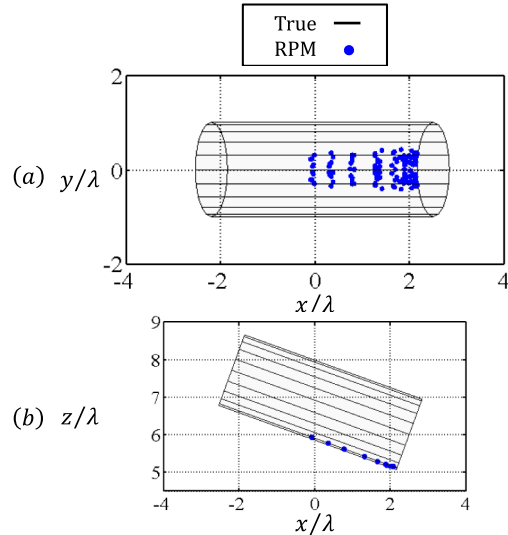

Fig. 25. Target boundary points estimated by the RPM method for the cylinder target. Solid lines: discrete expression of the true boundary.
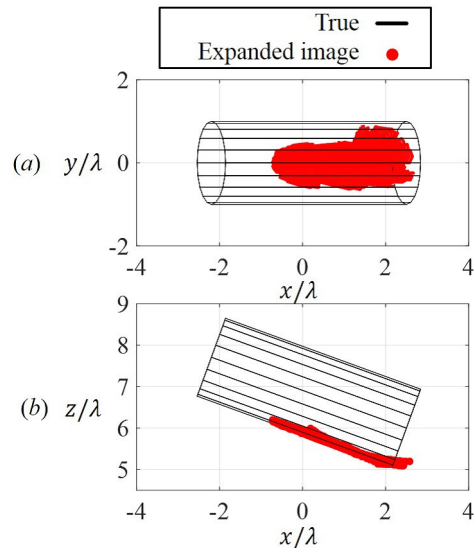

Fig. 26. Expansion result of the proposed method for the cylinder target. (a) Projection to the xy plane. (b) Cross section of the $y = 0$ plane.

for the proposed method, respectively. These quantitative evaluations also show that our method successfully expands the cylinder-shaped target, which guarantees an edge-preserving property.

VI. CONCLUSION

This paper proposed a novel 3-D image expansion method that incorporates the RPM method but exploits the fully polarimetric data set. In a time-series data analysis of fully polarimetric data, the co-polarization and cross-polarization data were strongly correlated with the radius and rotation angle of a single ellipsoid. By NN learning of the ellipsoid parameters, the target was accurately estimated from the time-series data only received by a single antenna. Next, to expand the reproduced image, we combined the RPM method with

This article has been accepted for inclusion in a future issue of this journal. Content is final as presented, with the exception of pagination.

12   IEEE TRANSACTIONS ON GEOSCIENCE AND REMOTE SENSING

single-ellipsoid estimation by the fully polarimetric data. By using multiple partial ellipsoidal surfaces to the RPM target points, we exploited the one-to-one correspondence between the target and range points, which makes us possible to connect the polarimetric data to each target point. In addition, to deal with a target having edges or ridges, our method adaptively change the expansion area with the curvature analysis provided by the RPM feature. Finally, in FDTD simulations, we verified that the image expansion ratio is much higher in the proposed method than in the original RPM method, even for decidedly nonellipsoidal target shapes, without serious accuracy degradation. The extrapolation level of the proposed method depends on the parameter ϕ_E in (12), which determines the extrapolation area of the partial ellipsoid. If we set ϕ_E larger, there is a risk for generating a false image deviated from the actual boundary. Then, the adjustment of the parameter ϕ_E is required to keep balance between the accuracy and the expansion effect. As a result, the expansion effect in the case of an ellipsoid target seems to be an interpolated image; this is because the reflection strength from an ellipsoid is comparatively smaller than that from a torus or cylinder object, where the signal strength is the one factor to determine the size of each fitted ellipsoid.

Note that the proposed method does not need to decompose co-polarization and cross-polarization components from the measured data, which are generally difficult in the nonplanar incident-wave case. This is because this method requires a relative quantity between the reference (training) signal and the received signal, in terms of the x and y components of electric fields. However, the accuracy of the polarimetric measurement would affect the final image in both the RPM and proposed method. It is also noted that the training data in the NN are only limited to an ellipsoid, then, to deal with the general boundary shape having a concave or saddle boundary; the training data from the object with such negative principal curvatures should be processed. It is our important future work. Further investigation on such an effect should be done in our future work through real experiments.

REFERENCES

[1] D. Mensa, G. Heidbreder, and G. Wade, "Aperture synthesis by object rotation in coherent imaging," *IEEE Trans. Nucl. Sci.*, vol. NS-27, no. 2, pp. 989–998, Apr. 1980.

[2] A. J. Devaney, "Time reversal imaging of obscured targets from multistatic data," *IEEE Trans. Antennas Propag.*, vol. 53, no. 5, pp. 1610–1660, May 2005.

[3] E. A. Marengo, F. K. Gruber, and F. Simonetti, "Time-reversal MUSIC imaging of extended targets," *IEEE Trans. Image Process.*, vol. 16, no. 8, pp. 1967–1984, Aug. 2007.

[4] J. M. Lopez-Sanchez and J. Fortuny-Guasch, "3-D radar imaging using range migration techniques," *IEEE Trans. Antennas Propag.*, vol. 48, no. 5, pp. 728–737, May 2000.

[5] J. Song, Q. H. Liu, P. Torrione, and L. Collins, "Two-dimensional and three-dimensional NUFFT migration method for landmine detection using ground-penetrating radar," *IEEE Trans. Geosci. Remote Sens.*, vol. 44, no. 6, pp. 1462–1469, Jun. 2006.

[6] F. Soldovieri, A. Brancaccio, G. Prisco, G. Leone, and R. Pierri, "A kirchhoff-based shape reconstruction algorithm for the multimonostatic configuration: The realistic case of buried pipes," *IEEE Trans. Geosci. Remote Sens.*, vol. 46, no. 10, pp. 3031–3038, Oct. 2008.

[7] T. Sakamoto, "A fast algorithm for 3-dimensional imaging with UWB pulse radar systems," *IEICE Trans. Commun.*, vol. E90-B, no. 3, pp. 636–644, Mar. 2007.

[8] S. Kidera, T. Sakamoto, and T. Sato, "Accurate UWB radar three-dimensional imaging algorithm for a complex boundary without range point connections," *IEEE Trans. Geosci. Remote Sens.*, vol. 48, no. 4, pp. 1993–2004, Apr. 2010.

[9] S. Kidera and T. Kirimoto, "Efficient three-dimensional imaging method based on enhanced range point migration for UWB radars," *IEEE Geosci. Remote Sens. Lett.*, vol. 10, no. 5, pp. 1104–1108, Sep. 2013.

[10] S. Kidera, T. Sakamoto, and T. Sato, "Super-resolution UWB radar imaging algorithm based on extended capon with reference signal optimization," *IEEE Trans. Antennas. Propag.*, vol. 59, no. 5, pp. 1606–1615, May 2011.

[11] R. Salman and I. Willms, "3D UWB radar super-resolution imaging for complex objects with discontinuous wavefronts," in *Proc. IEEE Int. Conf. Ultra-Wideband (ICUWB)*, Sep. 2011, pp. 346–350.

[12] S. S. Fayazi, J. Yang, and H.-S. Lui, "UWB SAR imaging of near-field object for industrial process applications," in *Proc. 7th Eur. Conf. Antennas Propagat. (EuCAP)*, Apr. 2013, pp. 2245–2248.

[13] H. Taki, S. Tanimura, T. Sakamoto, T. Shiina, and T. Sato, "Accurate ultrasound imaging based on range point migration method for the depiction of fetal surface," *J. Med. Ultrason.*, vol. 42, no. 1, pp. 51–58, Sep. 2014.

[14] Y. Abe, S. Kidera, and T. Kirimoto, "Accurate image expansion method using range points based ellipse fitting for UWB imaging radar," *IEICE Trans. Commun.*, vol. E95-B, no. 7, pp. 2424–2432, Jul. 2012.

[15] D. Damyanov, T. Schultze, I. Willms, and R. Salman, "Super-resolution feature extraction imaging algorithm for complex objects," in *Proc. IEEE IEEE Int. Conf. Ultra-WideBand (ICUWB)*, Sep. 2014, pp. 207–210.

[16] R. Salman, I. Willms, T. Sakamoto, T. Sato, and A. Yarovoy, "3D imaging of a manmade target with weak scattering centres by means of UWB-radar," in *Proc. IEEE IEEE Int. Conf. Ultra-WideBand (ICUWB)*, Sep. 2013, pp. 109–112.

[17] J. Kruk, C. P. A. Wapenaar, J. T. Fokkema, and P. M. Van den Berg, "Three-dimensional imaging of multicomponent ground-penetrating radar data," *Geophysics*, vol. 68, no. 4, pp. 1241–1254, 2003.

[18] A. G. Yarovoy, A. D. Schukin, I. V. Kaploun, and L. P. Ligthart, "High-resolution full-polarimetric video impulse radar for landmine detection," in *Proc. Int. Radar Conf.*, Oct. 2002, pp. 205–209.

[19] V. Kovalenko, A. Yarovoy, and L. P. Ligthart, "Polarimetric feature fusion in GPR for landmine detection," in *Proc. IEEE Int. Geosci. Remote Sens. Symp. (IGARSS)*, Jul. 2007, pp. 30–33.

[20] R. Salman and I. Willms, "Exploitation of polarimetry in short range 3D UWB-radar object imaging," in *Proc. Int. Conf. 3D Imag. (IC3D)*, Dec. 2012, pp. 1–7.

[21] S. Kidera, T. Sakamoto, and T. Sato, "High-resolution and real-time three-dimensional imaging algorithm with envelopes of spheres for UWB radars," *IEEE Trans. Geosci. Remote Sens.*, vol. 46, no. 11, pp. 3503–3513, Nov. 2008.

[22] S. Kidera, T. Sakamoto, and T. Sato, "A high-resolution imaging algorithm without derivatives based on waveform estimation for UWB radars," *IEICE Trans. Commun.*, vol. E89-B, no. 9, pp. 1487–1494, Sep. 2006.

[23] S. Kidera, T. Sakamoto, and T. Sato, "A robust and fast imaging algorithm with an envelope of circles for UWB pulse radars," *IEICE Trans. Commun.*, vol. E90-B, no. 7, pp. 1801–1809, Jul. 2007.

Ayumi Yamaryo received the B.E. and M.E. degrees in electronic engineering from The University of Electro-Communications, Tokyo, Japan, in 2013 and 2015, respectively.

She joined Mitsubishi Electric Corporation, Tokyo, in 2015.

Tatsuo Takatori received the B.E. degree in communication engineering and informatics from The University of Electro-Communications, Tokyo, Japan, in 2016, where he is currently pursuing the M.E. degree with the Graduate School of Informatics and Engineering.

His research interests include advanced radar signal processing for ultrawideband radar systems.

Shouhei Kidera (M'11) received the B.E. degree in electrical and electronic engineering and the M.I. and Ph.D. degrees in informatics from Kyoto University, Kyoto, Japan, in 2003, 2005, and 2007, respectively.

He was a Visiting Researcher with the Cross-Disciplinary Electromagnetics Laboratory, University of Wisconsin–Madison, Madison, WI, USA, in 2016. He has been with the Graduate School of Informatics and Engineering, The University of Electro-Communications, Tokyo, Japan, since 2009, where he is currently an Associate Professor. His research interests include advanced radar signal processing or electromagnetic inverse scattering issue for ultrawideband 3-D sensor or biomedical applications.

Dr. Kidera is a member of the Institute of Electronics, Information, and Communication Engineers of Japan and the Institute of Electrical Engineering of Japan. He was a recipient of the 2012 Ando Incentive Prize for the Study of Electronics, the 2013 Young Scientist's Prize by the Japanese Minister of Education, Culture, Sports, Science and Technology, and the 2014 Funai Achievement Award.

Tetsuo Kirimoto (M'91–SM'97) received the B.S., M.S., and Ph.D. degrees in communication engineering from Osaka University, Osaka, Japan, in 1976, 1978, and 1995, respectively.

From 1978 to 2003, he was with Mitsubishi Electric Corporation, Tokyo, Japan, to study radar signal processing.From 1982 to 1983, he was a Visiting Scientist with the Remote Sensing Laboratory, The University of Kansas, Lawrence, KS, USA. From 2003 to 2007, he was with The University of Kitakyushu, Kitakyushu, Japan, as a Professor. Since 2007, he has been with The University of Electro-Communications, Tokyo, where he is currently a Professor with the Graduate School of Informatics and Engineering.His research interests include digital signal processing and its application to various sensor systems.

Dr. Kirimoto is a member of the Institute of Electronics, Information, and Communication Engineers of Japan and The Society of Instrument and Control Engineers of Japan.